Optics Communications 503 (2022) 127422

Contents lists available at ScienceDirect

Optics Communications

journal homepage: www.elsevier.com/locate/optcom

Investigation of noise amplification questions in satellite jitter detected from CCDs' parallax observation imagery: A case for 3 CCDs

Haiqiu Liu [a,*], Huimin Ma [a], Qixing Tang [b], Dong Wang [c]

[a] School of Information and Computer, Anhui Agricultural University, 130 Changjiang West Road, Hefei, 230036, China
[b] School of Engineering, Anhui Agricultural University, 130 Changjiang West Road, Hefei, 230036, China
[c] Changchun Institute of Optics, Fine Mechanics and Physics, Chinese Academy of Sciences, 3888 Nanhu road, Changchun, 130033, China

ARTICLE INFO

Keywords:
Satellite jitter detection
Parallax observation images
Noise-amplifying frequency
Error transfer coefficient
Offset
CCD

ABSTRACT

Parallax observations from adjacent CCDs have been applied to detect satellite jitter, and the highest detectable jitter frequency reaches up to half CCDs image line frequency, among which, however, not all frequencies' jitter could be detected accurately. Jitter error mainly comes from the noise in offset data. In this research, it is found that at some frequencies the noise is amplified significantly, leading to seriously deviated jitter components and even unreliable jitter results. This research focuses on the noise-amplifying questions in jitter detection and explores what CCD parameters determine them. Firstly, the error transfer coefficients (ETC) between jitter and offset is derived, and the frequencies are divided into three categories: blind frequencies, noise-amplifying frequencies and noise-suppressing frequencies. Secondly, for two adjacent CCDs, formulas are established to determine their blind frequencies and noise-amplifying bands, which indicate that it is the two CCDs' image line time t_r and the distance l between the two CCDs' first lines that determine their blind frequencies and noise-amplifying bands. The reciprocal of the product of t_r and l is defined as the fundamental frequency F of the CCD pair. As a result, the blind frequencies and noise-amplifying bands both reoccur with a period of fundamental frequency F, but unlike those isolated bind frequencies, the noise-amplifying bands span much wider, up to nearly 1/3 jitter bandwidth. Thirdly, for three adjacent CCDs forming two CCD pairs, aliasing between the two pairs' noise-amplifying bands is first proven to be inevitable and reoccurs in cycles. Formulas are then established to extract the aliasing components and compute the aliasing period length. Experiments and simulations are conducted to test the constructed theories. Results show that the RMSE is 7.127×10^{-5} Hz for blind frequencies formulas, and the RRMSEs are 0.0051% for noise-amplifying bands' period formulas, 0.0033% for aliasing period, and 1.2610% for noise-amplifying bandwidth, proving that the established formulas could generate reliable results for the blind frequencies, noise-amplifying bands and their aliasing components of three adjacent CCDs. Our studies are expected to help analyze more CCDs' noise-amplifying problems and provide a prospect to reduce their impact on jitter detection by optimizing CCD parameter values.

1. Introduction

Various vibrations seriously disturb the stability of satellite platform. Although most of the energy can be suppressed or isolated, there is still some jitter remaining [1–3]. Satellite jitter usually possesses relatively smaller energy, but spans a wider bandwidth of hundreds of Hertz [4–6]. Meanwhile, satellite jitter can be transmitted to cameras, causing additional image motion on focal planes and eventually distorting images [7,8]. As a result, it has become essential for high-resolution satellites with long focal length to detect the jitter accurately [9].

Several approaches have been proposed to detect satellite jitter. The first method is to use high-performance attitude-measuring sensors that can collect satellite jitter with a high sampling rate and high accuracy. An Angular Displacement Assembly (ADA) is installed on Landsat-7 spacecraft to measure its jitter at a rate of 500 Hz [10], in addition, Chinese Yaogan-26 satellite estimated its jitter within 0.2~450 Hz by equipping a high-performance angular displacement sensor [3]. Nevertheless, it is still inaccessible for many satellites to install a High-performance attitude-measuring sensors [11], which limits the application of this method in jitter detection.

The second approach depends on an additional matrix imaging sensor mounted beside main imaging sensors to catch the movement of image points. Janschek et al. took advantage of the high sampling rate of matrix imaging sensors to catch wide-bandwidth image motion information [12–14].

* Corresponding author.
E-mail address: lhq@ahau.edu.cn (H. Liu).

https://doi.org/10.1016/j.optcom.2021.127422
Received 7 June 2021; Received in revised form 26 August 2021; Accepted 29 August 2021
Available online 1 September 2021

The third approach is to use adjacent imaging sensors, which are configured in staggered splicing or parallel arrangement on a push-broom satellite focal plane, to acquire parallax observation images taken at slightly different times. Mattson et al. obtained the jitter information by using HiRISE camera's several adjacent CCDs and estimated the jitter of LROC-NAC camera from NACL and NACR images [15,16]. Tong et al. measured the distortions of the ZY-3 satellite from multispectral and three-line-scanning imagery [17,18], Zhen et al. reconstructed the along-track attitude jitter of ZY-3 satellite based on relative residuals of tri-band multispectral imagery [19]. Teshima and Iwasaki adopted adjacent parallax bands to acquire ASTER short-wave infrared images and constructed its attitude information [20,21]. Sun et al. discovered Chinese mapping satellite-1 jitter at 0.1 Hz and 0.6 Hz [22]. Mumtaz and Palmer detected the attitude data from the inter-image offsets between a pair of slightly canted sensors [23]. Liu et al. evaluated the jitter of Chinese ZY-3 Satellite from image discrepancies [24]. Zhu et al. detected GaoFen-1 02/03/04 Satellites jitter based on parallax observation multispectral sensor images [25]. In addition, the authors of this paper take advantage of engineering parameters and staggered CCDs to reconstruct Chinese satellite jitter information [26].

The third method has received more attention due to its ability to detect jitter from parallax observation images taken by adjacent imaging sensors, rather than by adding extra high-performance attitude-measuring devices or additional matrix imaging sensors. The error in jitter detection mainly comes from offset noise and the ETC between them [26]. We found that the ETC values approach infinity at some frequencies where the corresponding jitter components cannot be detected, and we call them as blind frequencies. More importantly, those ETC values near blind frequencies are also extremely large, leading to remarkable amplifications of the offset noise, and even resulting in unreliable jitter components. Unlike those isolated blind frequencies, the frequencies with large ETC values span much wider bands, and causing significant deviations in jitter results. The noise-amplifying problem in jitter detection is worthy of attention.

This study focuses on the noise-amplifying issues in jitter detection, establish formulas to calculate the noise-amplifying frequencies, finds out what patterns they follow, and most importantly, reveals what CCD parameters determine the noise-amplifying frequencies in jitter detection and the quantitative relationship between them.

The rest of this paper is organized as follows. Following the introduction, Section 2 provides evidence for noise-amplifying problem in jitter detection. In Section 3, for two adjacent CCDs, coefficient of error transfer is first derived to measure how much offset noise is amplified after transferring to jitter. Formulas are established to determine the blind frequencies and noise-amplifying bands in jitter detection and reveal the relationship between them and CCD parameters. Knowing the central frequency of a noise-amplifying band and the bandwidth it spans allows us to pinpoint its location, so two formulas are established to compute the central frequency of a noise-amplifying band and its bandwidth. For three adjacent CCDs forming two CCD pairs, aliasing between two pairs' noise-amplifying bands is proven to be inevitable in Section 4. Following this, formulas are subsequently developed to extract the aliasing components and determine the period of aliasing bandwidth in Section 5. Finally, experiments and numerical simulations are performed in Section 6 to validate the constructed theories. Discussions and conclusions are given in Section 7 and Section 8.

2. Evidence for noise-amplifying issues in jitter detection

2.1. Fundamental of jitter detection from CCD pair's parallax observation imagery

A linear CCD is usually equipped with several bands, and one of the most commonly used combinations are panchromatic, red, green and blue bands. In each band, lines of pixels are made to support the possible multilevel integration, as shown in Fig. 1(a), where R_1 denotes the first line of pixels in each band. In the scanning direction, distance exists between the first lines of the same bands from two CCDs, as shown in Fig. 1(b), where P, R, G and B denote the panchromatic band, red band, green band and blue band, respectively, l_P, l_R, l_G and l_B represent the distances of the first lines between two CCDs' panchromatic bands, red bands, green bands and blue bands, respectively. The panchromatic band usually has a higher space resolution than the other three bands, thereby the parallax observation images in panchromatic band are the most commonly used in satellite jitter detection. In the following sections, images refer to the panchromatic images unless otherwise specified, similarly, "the distance between the first lines of two adjacent CCDs' means the distance between the first lines of two adjacent CCDs' panchromatic bands, so the symbol l_P is replaced with l for easy representation.

CCDs mounted on a pushbroom satellite focal plane are usually configured in two ways [27–30]: staggered splicing or parallel arrangement, as shown in Fig. 2, both the two configurations form overlapping pixels, generating overlapping footprints in object plane. However, due to the distance of the first lines between two adjacent CCDs in the scanning direction, their overlapping pixels scan the same object with a fixed time interval, while all pixels are affected by the same jitter simultaneously, resulting in an offset between the same object's position in the two overlapping images. So offset in images can be written as Eq. (1).

$$g(t + l \times t_r) = j\left(t + l \times t_r\right) - j\left(t\right), \quad 0 \le t \le T - l \times t_r \tag{1}$$

Where l denotes the difference between the first lines of two adjacent CCDs in the scanning direction, t_r is the two CCDs' identical image line time, note that the two CCDs used for detecting jitter have to be set in the same image line time. $j(t)$ and $j(t+ l\times t_r)$ denote the jitter values at time t and $(t+ l\times t_r)$, $g(t+ l\times t_r)$ represents the offset between the image obtained by the CCD $2^{\#}$ at time t and that obtained by the CCD $1^{\#}$ at time $(t+ l\times t_r)$, and T is the duration of a shooting mission.

2.2. Evidence in Chinese xx-1 satellite jitter results

Due to lack of true values of on-orbit satellite jitter, it is difficult to evaluate the accuracy of jitter detected from parallax observation imagery. Nevertheless, the detected on-orbit satellite jitter results still present an evidence for noise-amplifying issues.

Experiments are performed on Chinese xx-1 satellite to prove the existence of noise-amplifying issues in jitter detection. Five CCDs are mounted on the satellite focal plane and any two adjacent CCDs overlap each other by 40 columns of pixels, and we pick the middle two adjacent CCDs to detect satellite jitter. With typical image line time of 65 microseconds and the distance between two adjacent CCDs' first lines of 3480 lines, over 900,000 lines of parallax observation images are obtained from the two adjacent CCDs in a mission of about 30 s started at 10:34 AM April 12, 2012, using which the satellite jitter is estimated with the assist of its on-orbit engineering parameters by adopting the method in [26].

Results are shown in Fig. 3. In the cross-track direction, large numbers of peaks appear in the amplitude–frequency jitter curve (marked by red triangles), and they are located at 0.05 Hz, 4.38 Hz, 8.81 Hz, 13.27 Hz, 17.64 Hz, *etc*. as shown in Fig. 3(a) and Fig. 3(b). Similarly, peaks also occur in the down-track satellite jitter curve, as shown in Fig. 3(d) and Fig. 3(e), and they are located at 0.02 Hz, 4.39 Hz, 8.86 Hz, 13.27 Hz, 17.70 Hz, *etc*. It can be seen that all the peak frequencies in both cross-track and down-track directions are well fitted by the function $y = 4.42x$ with $R^2 = 1$, as shown in Fig. 3(c) and Fig. 3(f). This coincidence raises two questions: are these peaks true jitter components or just error? Why are they all located integer multiples of 4.42 Hz?

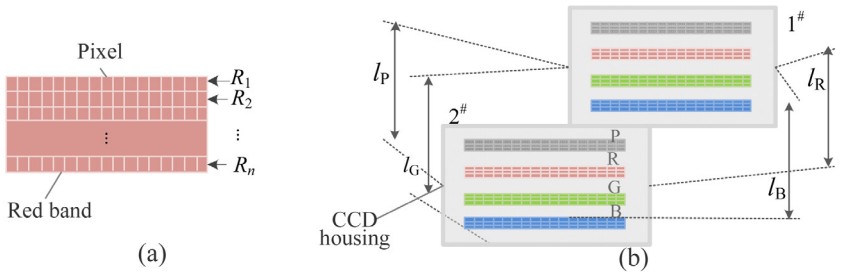

Fig. 1. Bands in a linear CCD and the first line in a band. (a) A band with several lines of pixels to support the possible multilevel integration, R_1, R_2 and R_n are the first, second and nth line of pixels. (b) Two adjacent CCDs with four bands, P, R, G and B denote the panchromatic band, red band, green band and blue band, respectively, l_P, l_R, l_G and l_B represent the distances of the first lines between two CCDs' panchromatic bands, red bands, green bands and blue bands, respectively.

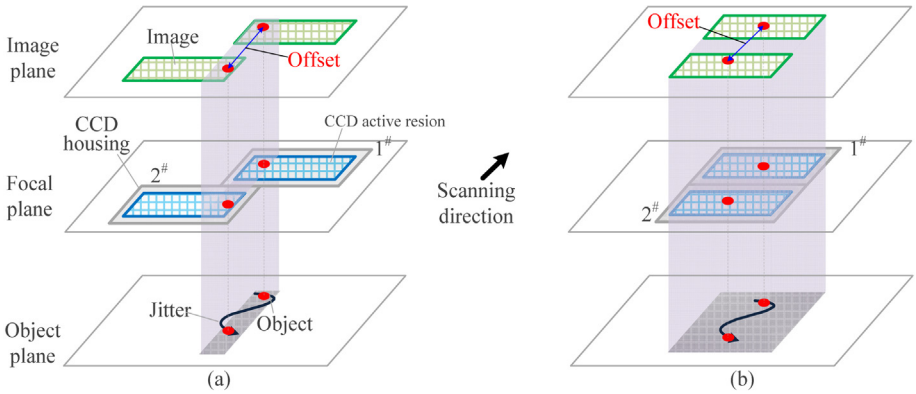

Fig. 2. Imaging process of two adjacent CCDs configured as (a) staggered splicing, (b) parallel arrangement.

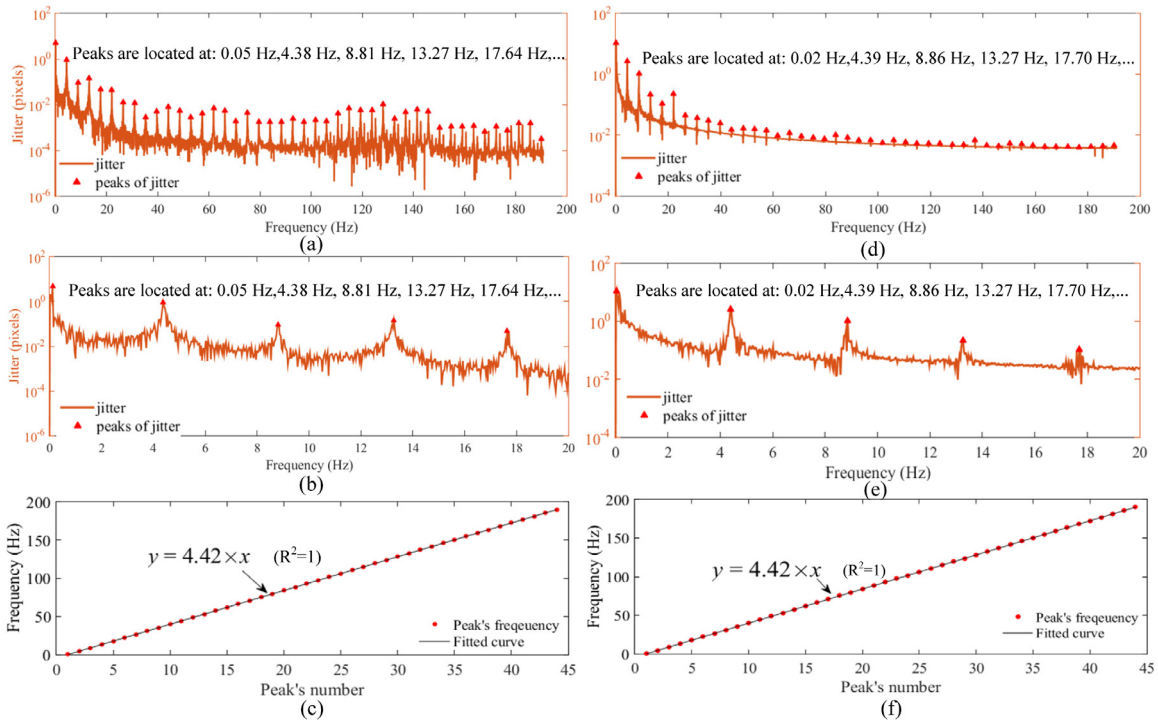

Fig. 3. Chinese xx-1 satellite jitter results in frequency domain. (a) Amplitude–frequency curve of jitter within [0 192 Hz] in cross-track direction. (b) 0–20 Hz part of Fig. 3(a). (c) Peaks' frequencies in Fig. 3(a). (d) Amplitude–frequency curve of jitter within [0 192 Hz] in down-track direction. (e) 0–20 Hz part of Fig. 3(d). (f) Peaks' frequencies in Fig. 3(d).

2.3. Evidence in numerical simulations

In order to investigate whether the peaks in Chinese xx-1 satellite jitter results are true jitter components or just an error, numerical simulations are conducted with the parameters of Chinese xx-1 satellite: the typical image line time t_r is 65 microseconds, the distance between two adjacent CCDs' first lines l is 3480 lines, and every 40 lines × 40 columns pixels form an cell to produce an offset data by image

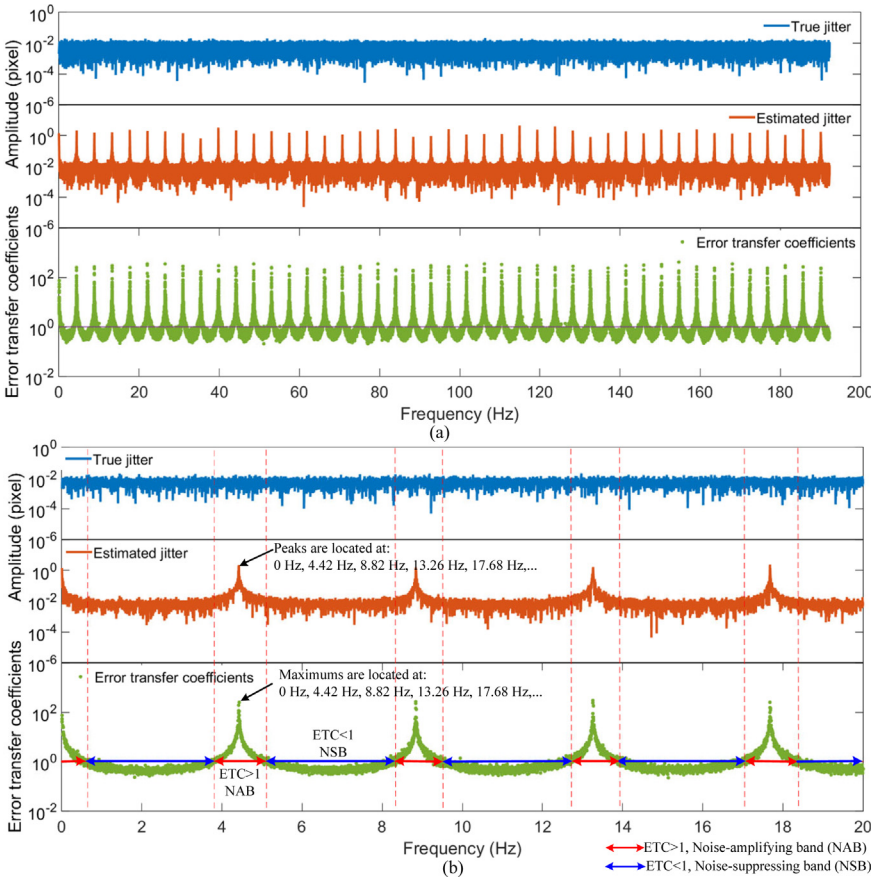

Fig. 4. Comparison between estimated jitter and their true values and the transfer coefficients between jitter error and offset noise. (a) Comparison within [0 192 Hz]. (b) Comparison within [0 20 Hz].

matching. Theoretically, the parallax observation images can detect the jitter up to $1/(2u{\times}t_r) = 1/2/40/65$ μs = 192 Hz according to Nyquist sampling theorem. Plus, the main jitter component of Chinese xx-1 satellite has an amplitude of ~6 pixels. So a band-limited white noise with a mean value of −0.003 pixels and a variance of 6.733 square pixels in [0 192 Hz] is used to simulate the true jitter, and the corresponding offset data is calculated by using Eq. (1). Following this, the offset is mixed with the white noise σ_{offset} whose mean and variance are 0.004 pixels and 1.002 square pixels, and the jitter results were then obtained by using the method in reference [26].

Results are shown in Fig. 4, the blue, orange and green curves represent the jitter's true values, estimated values and the transfer coefficients between jitter error and offset noise, respectively. Just like the Chinese xx-1 satellite jitter results in Fig. 3, large peaks appear in the estimated jitter curve, which are located at 0 Hz, 4.42 Hz, 8.84 Hz, 13.26 Hz, 17.68 Hz, *etc*. and their fitted function is $y = 4.42x$ with $R^2 = 1$, as shown in Table 1. The ETCs at the peaks' frequencies are extremely large. Obviously, the peaks in the simulations are not real jitter components, but the significantly amplified noise by the extremely large ETCs. Since the simulations use the same parameters values (l and t_r) with Chinese xx-1 satellite experiments, their peak frequencies in jitter results are very close to each other, and they share the same fitted functions with $R^2 = 1$, as shown in Table 1, it is reasonable to believe that, just like the simulations, the peaks in the experiments in Fig. 3 are also not real jitter components, but the seriously amplified noise by large ETCs. It should be noticed that, besides the ETC peaks, those ETC values near the peaks are also extremely large, leading to serious amplifications of the offset noise, and resulting in jitter's significant deviations, as shown in Fig. 4(b).

Therefore, large numbers of peaks appear in both Chinese xx-1 satellite jitter experiments and simulations, results show that the jitter peaks are not real jitter components, but the seriously amplified noise by the extremely large ETCs at peaks frequencies. Both the simulations and experiments confirm the existence of noise-amplifying issues in satellite jitter. But why are they all located around the integer multiples of 4.42 Hz? Is 4.42 Hz related to any CCD parameters?

3. Determining the noise-amplifying bands for one CCD pair

At least one CCD pair is required to produce parallax observation images for detecting satellite jitter. Here we first analyze the noise-amplifying issues for one CCD pair and then use it to explore the noise-amplifying bands of two CCD pairs which are more complicated.

Since the error of satellite jitter mainly comes from offset data noise and ETC [26], we adopt mathematical method to derive the ETC between jitter and offset, which allows to measure how much the offset noise is amplified, and then extract those noise-amplifying frequencies.

3.1. Deriving error transfer coefficient between jitter and offset data

Satellite jitter shows an obvious sinusoidal pattern [9], so the offset can be substituted by sine functions as Eq. (2).

$$g(t) = \sum_{k=1}^{K} B_k^g \sin\left(2\pi f_k^g t + \sigma_k^g\right), \qquad k = 1, 2, \ldots, K \tag{2}$$

Where f_k^g, B_k^g and σ_k^g are the frequency, amplitude and initial phase of the kth sinusoidal component of offset $g(t)$, respectively. According to Eqs. (1) and (2), the frequency and amplitude of jitter can be expressed as:

$$f_k^j = f_k^g, \qquad k = 1, 2, \ldots, K \tag{3}$$

Table 1
Peak locations in numerical simulations and Chinese xx-1 satellite jitter experiments.

	CCD parameters	Peak locations (Hz)	Fitted functions
Experiments	l = 3480 lines t_r = 65 μs	0.05, 4.38, 8.81, 13.27, 17.64, *etc.* (Cross-track)	$y = 4.42x$, $R^2 = 1$
Simulations		0.05, 4.39, 8.86, 13.27, 17.70, *etc.* (Down-track)	$y = 4.42x$, $R^2 = 1$
		0.00, 4.42, 8.84, 13.26, 17.68, *etc.*	$y = 4.42x$, $R^2 = 1$

$$B_k^j = \frac{B_k^g}{\left|2\sin\left(\pi \cdot l \cdot t_r \cdot f_k^j\right)\right|}, \qquad k = 1, 2, \ldots, K \tag{4}$$

Where l the distance between the first lines of two adjacent CCDs, t_r represents their identical image line time, f_k^j and B_k^j are the frequency and amplitude of the kth sinusoidal component of the jitter, respectively. According to Eq. (4), the relationship between jitter error and offset noise can be expressed as:

$$\delta_{B_k^j} = \frac{dB_k^j}{dB_k^g} \cdot \delta_{B_k^g} = \frac{\delta_{B_k^g}}{\left|2\sin\left(\pi \cdot l \cdot t_r \cdot f_k^j\right)\right|}, \qquad k = 1, 2, \ldots, K \tag{5}$$

Where $\delta_{B_k^j}$ and $\delta_{B_k^g}$ denote the jitter error and offset noise, respectively.

For two adjacent CCDs, we define the reciprocal of the product of their image line time t_r and the distance l between their first lines as their fundamental frequency F, as shown in Eq. (6).

$$F = \frac{1}{l \cdot t_r} \tag{6}$$

So, the error transfer coefficient $\kappa(l, t_r, f)$ between the jitter error and offset noise can be constructed as Eq. (7), where the symbol f_k^j is replaced with f for easy representation, and the error transfer coefficient $\kappa(l, t_r, f)$ can be expressed as $\kappa(F, f)$.

$$\kappa\left(l, t_r, f\right) = \kappa\left(F, f\right) = \frac{\delta_{B_k^j}}{\delta_{B_k^g}} = \left|\frac{1}{2\sin\left(\pi \cdot l \cdot t_r \cdot f\right)}\right| = \left|\frac{1}{2\sin\left(\frac{\pi \cdot f}{F}\right)}\right| \tag{7}$$

Since Eq. (7) is a cosecant function, the ETC is a periodic function of frequencies, and its period length equals to the CCD pair's fundamental frequency F. In each cycle, ETC is axisymmetric about its central frequency, reaches infinity at its center and gradually decreases as the frequency moves away from its center.

3.2. Establishing formulas to determine blind frequencies and noise-amplifying bands

As we know, the denominator in the Eq. (7) cannot be equal to zero, so the jitter at those frequencies making the denominator in the Eq. (7) zero cannot be detected from parallax observation images. We call these frequencies as "blind frequencies" of the two adjacent CCDs, and can be written as Eq. (8).

$$\left\{f_b\right\} = n \times F = \{0, F, 2F, 3F, \ldots\}, \qquad n = 0, 1, 2, \ldots \tag{8}$$

Where $\{f_b\}$ denotes the blind frequencies of two adjacent CCDs, F is the fundamental frequency of the CCD pair. Obviously, the bind frequencies in jitter detection are isolated and reoccur every fundamental frequency of F.

It can be seen that, for two adjacent CCDs, the ETCs at integer multiples of their fundamental frequency approach infinity, which causes that the corresponding jitter components cannot be detected from their parallax observation images. In addition, the frequencies very close to blind frequencies also produce large ETCs, resulting in serious jitter error and even unreliable jitter components, as shown in Eq. (9).

$$\begin{aligned}\kappa\left(F, (n+\Delta n) \times F\right) &= \left|\frac{1}{2\sin\left[\pi \cdot \frac{1}{F} \cdot (n+\Delta n) \times F\right]}\right| \\ &= \frac{1}{|2\sin(\Delta n \cdot \pi)|} \gg 1, \quad \Delta n \to 0, \quad n = 0, 1, 2, \ldots\end{aligned} \tag{9}$$

ETC and offset noise are the main factors of jitter error. Offset is acquired by matching two parallax observation images, and its accuracy is related to image content. For the content with obvious differences (e.g. town), the offset accuracy can reach to pixel or sub-pixel levels, while for the content with no obvious differences (e.g. water body, mountain or desert), the offset noise get worse [31]. The truth is that most of satellite images cover a lot of areas that have no conspicuous differences, leading to an average offset noise more likely worse than 1 pixel. As we know, satellite jitter is a kind of vibration with large frequency span but very small amplitude, for example, the main jitter component of Chinese xx-1 satellite only has an amplitude of ~6 pixels [26]. An error more than 1 pixel will seriously deteriorate the jitter results. Under the average offset noise probably larger than 1 pixel, it is hoped for the ETC to be no more than 1 to produce a relatively reliable jitter results.

ETC varies with frequencies, those continuous frequencies with ETC>1 is classified as a noise-amplifying band, and those with ETC<1 is classified as a noise-suppressing band. We try to get knowledge of noise-amplifying bands in ETC to explain the phenomena in Section 2.

According to Eq. (9), the noise-amplifying frequencies can be expressed as:

$$\begin{aligned}\left\{f_a\right\} &= \{f \mid ETC > 1\} \\ &= \left(0, \frac{F}{6}\right) \cup (F - F/6, F + F/6) \cup (2F - F/6, 2F + F/6) \\ &\quad \cup (3F - F/6, 3F + F/6) \cdots\end{aligned} \tag{10}$$

Where $\{f_a\}$ denotes the set of noise-amplifying frequencies for one CCD pair, F is the CCD pair's fundamental frequency, and the operator $\cup$ returns the result of union operation.

According to Eqs. (8) and (10), the noise-amplifying frequencies are located around blind frequencies, and those continuous noise-amplifying frequencies around a blind frequency form a noise-amplifying band, so the nth noise-amplifying band $B(n, l, t_r)$ around the nth blind frequency can be written as:

$$\begin{aligned}B\left(n, l, t_r\right) &= \begin{cases} \left(0, \frac{1}{6 \times l \times t_r}\right) \\ \left(\frac{n}{l \times t_r} - \frac{1}{6 \times l \times t_r}, \frac{n}{l \times t_r} + \frac{1}{6 \times l \times t_r}\right) \end{cases} \\ &= \begin{cases} \left(0, \frac{F}{6}\right), & n = 0 \\ \left(n \cdot F - \frac{F}{6}, n \cdot F + \frac{F}{6}\right), & n = 1, 2, 3, \ldots \end{cases}\end{aligned} \tag{11}$$

Just like the isolated bind frequencies, the noise-amplifying bands, except the 0th one, also reappear with a cycle of F. So the period length of blind frequencies and noise-amplifying bands can be written as:

$$p_b\left(l, t_r\right) = p_n\left(l, t_r\right) = \frac{1}{l \times t_r} = F \tag{12}$$

Where $p_b(l, t_r)$ and $p_n(l, t_r)$ denote the period length of blind frequencies and noise-amplifying bands, respectively.

For Chinese xx-1 satellite with the CCD parameters: t_r = 65 μs and l = 3480 lines, its fundamental frequency F=1/(l×t_r)=1/(3480×65×10^{-6})≈4.42 Hz and its blind frequencies are f_b=4.42×n, n=0, 1, 2, …, according to Eqs. (6) and (8), as shown in Fig. 5. The blue curve is the ETC values calculated by the established formula of Eq. (7), and the green dots are the ETC values from the numerical simulation in Section 2.3. The green dots are evenly distributed around the blue curve, and they share the same blind frequencies. It can be seen that the established formula for blind frequencies could explain why the peaks

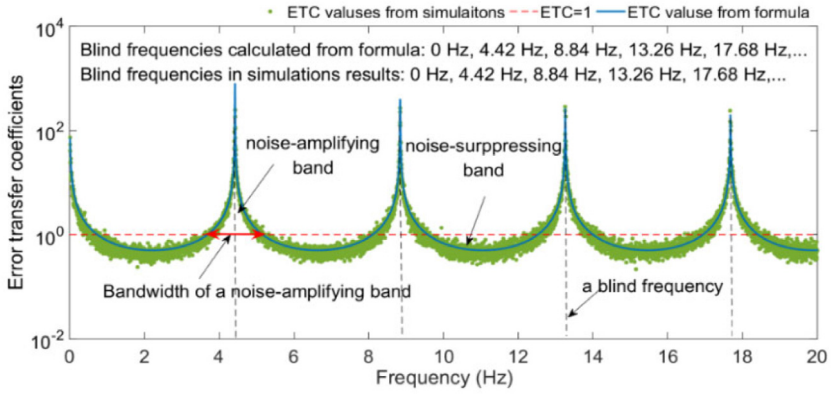

Fig. 5. Comparison between the ETC calculated by the established formula (blue curve) and its estimated values acquired in the simulations in Section 2.3 (green dots).

in Chinese xx-1 satellite jitter results are all located at integer multiples of 4.42 Hz, and it is the image line time t_r and the first lines distance l that determine the fundamental frequency of 4.42 Hz.

Therefore, both blind frequencies and noise-amplifying frequencies exist in the jitter detected from a CCD pair's parallax observation images. The jitter at blind frequencies are undetectable, while noise-amplifying frequencies refer to those where ETC >1, among which some frequencies' ETCs are extremely large, leading to significantly deviated jitter components. Formulas are established to calculate blind frequencies and noise-amplifying bands in jitter detection, which indicate that it is the two CCDs' image line time t_r and the distance l between their first lines that determine the blind frequencies and noise-amplifying bands. We define the reciprocal of the product of t_r and l as fundamental frequency F. Both blind frequencies and noise-amplifying bands reoccur with a cycle of fundamental frequency F. But unlike the isolated blind frequencies, a noise-amplifying band span much wider.

3.3. Calculating the central frequency and bandwidth of a noise-amplifying band

Knowing the central frequency of a noise-amplifying band and how wide it spans allows to locate it exactly, so two formulas are established to compute the central frequency of a noise-amplifying band and its bandwidth.

For a CCD pair, its noise-amplifying band reappears with a cycle of its fundamental frequency F, and the ETC in a noise-amplifying band is axisymmetric about its center, so the central frequencies of noise-amplifying bands are located at integer multiples of the fundamental frequency F, as shown in Eq. (13).

$$c\left(n,l,t_r\right)=0.5\times\left[\left(\frac{n}{l\times t_r}-\frac{1}{6\times l\times t_r}\right)+\left(\frac{n}{l\times t_r}+\frac{1}{6\times l\times t_r}\right)\right]$$
$$=\frac{n}{l\times t_r}=n\times F\,,\quad n=1,2,3,\ldots \tag{13}$$

Where $c(n,l,t_r)$ denotes the central frequency of the nth noise-amplifying band of two CCDs with the parameters of l and t_r. Since the 0th noise-amplifying band is not axisymmetric about its center, as shown in Fig. 5, its center is not given in Eq. (13).

Similarly, the bandwidth of a noise-amplifying band equals to 1/3 of their fundamental frequency F, as shown in Eq. (14), where $w(n,l,t_r)$ denotes the bandwidth of the nth noise-amplifying band of two CCDs with the parameters of l and t_r.

$$w\left(n,l,t_r\right)=\begin{cases}\dfrac{1}{6\times l\times t_r}=\dfrac{F}{6}, & n=0\\ \left[\left(\dfrac{n}{l\times t_r}+\dfrac{1}{6\times l\times t_r}\right)-\left(\dfrac{n}{l\times t_r}-\dfrac{1}{6\times l\times t_r}\right)\right] & \\ \quad=\dfrac{1}{3\times l\times t_r}=\dfrac{F}{3}, & n=1,2,3,\ldots\end{cases} \tag{14}$$

It can be seen that, unlike the isolated blind frequencies, a noise-amplifying band span much wider up to 1/3 F, thereby all the noise-amplifying bands total up to nearly 1/3 jitter bandwidth, which threaten the accuracy of jitter detection seriously.

4. Inevitable aliasing between two CCD pairs' noise-amplifying bands

4.1. Establishing formulas to calculate aliasing bandwidth

Three adjacent CCDs are usually configured in two ways, as shown in Fig. 6. 1# and 2# CCDs form the first pair and the distance between their first lines is l_1. 2# and 3# CCDs form the second pair and their first lines distance is l_2. The three CCDs have to work in the same image line time t_r. Let $r=l_2/l_1$, $r\geq1$, the two CCD pairs' fundamental frequencies can be written as $F_1=1/(l_1\times t_r)$ and $F_2=1/(l_2\times t_r)=F_1/r$ according to Eq. (6). If the two pairs of CCDs are configured with different parameter values, namely $l_1\neq l_2$, thus $F_1\neq F_2$.

Three adjacent CCDs form two pairs of CCDs, and they have their own specific sets of noise-amplifying bands, and can be written as Eqs. (15) and (16).

$$B_1\left(n_1,l_1,t_r\right)=\begin{cases}\left(0,\dfrac{1}{6\times l_1\times t_r}\right), & n_1=0\\ \left(\dfrac{n_1}{l_1\times t_r}-\dfrac{1}{6\times l_1\times t_r},\dfrac{n_1}{l_1\times t_r}+\dfrac{1}{6\times l_1\times t_r}\right), & n_1=1,2,3,\ldots\end{cases} \tag{15}$$

$$B_2\left(n_2,l_2,t_r\right)=\begin{cases}\left(0,\dfrac{1}{6\times l_2\times t_r}\right), & n_2=0\\ \left(\dfrac{n_2}{l_2\times t_r}-\dfrac{1}{6\times l_2\times t_r},\dfrac{n_2}{l_2\times t_r}+\dfrac{1}{6\times l_2\times t_r}\right), & n_2=1,2,3,\ldots\end{cases} \tag{16}$$

Where $B_1(n_1,\ l_1,\ t_r)$ is the n_1th noise-amplifying band of the first CCD pair, and $B_2(n_2,\ l_2,\ t_r)$ is the n_2th noise-amplifying band of the second CCD pair. An example is used to illustrate how two noise-amplifying bands alias. Parameters are as follows: l_1 = 3480 lines, l_2 = 3810 lines, t_r = 65 microseconds. The two pairs' ETCs are calculated by using Eq. (7) and results are shown in Fig. 7(a). The green and blue curves denote the ETCs of the two CCD pairs, their aliasing bandwidth is shown in Fig. 7(b).

Two noise-amplifying bands from different CCD pairs perhaps alias with each other, and the aliasing bandwidth varies with the distance between its two original bands' centers. If the distance is less than half of the two total bandwidths, partial aliasing occurs (as shown in Fig. 7(d)), if greater, no aliasing (as shown in Fig. 7(e)), and if its two original noise-amplifying bands share the same central frequency, they alias totally (as shown in Fig. 7(c)). So the aliasing bandwidth can be expressed as in Box I.

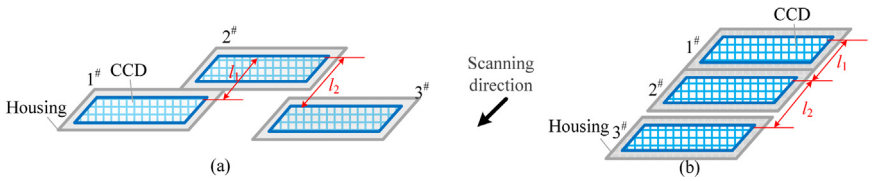

Fig. 6. Three adjacent CCDs' configuration with different layout parameter values. (a) Staggered splicing, (b) Parallel arrangement.

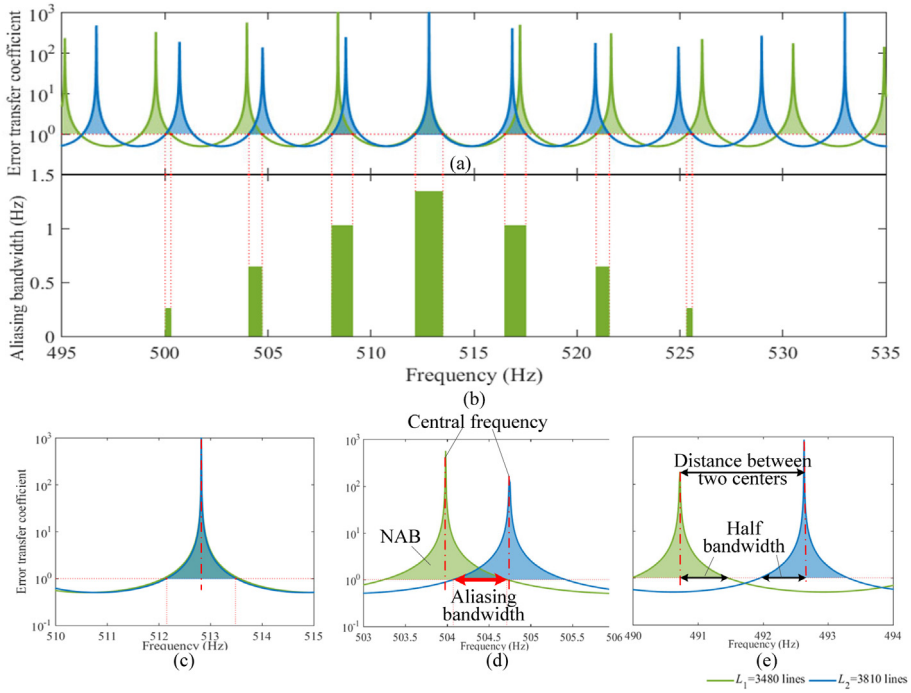

Fig. 7. Aliasing of two CCD pairs' noise-amplifying bands with l_1 = 3480 lines and l_2 = 3810 lines. (a) Error transfer coefficients of the two CCD pairs. (b) Aliasing bandwidth. Two noise-amplifying bands are (c) totally aliased, (d) partially aliased and (e) not aliased.

$$w_{1,2}^{als}(n_1,n_2,l_1,l_2,t_r) = \begin{cases} 0 & , \quad \left|c_1(n_1,l_1,t_r) - c_2(n_2,l_2,t_{r2})\right| > \frac{1}{6}\cdot\left(\frac{1}{l_1\times t_r}+\frac{1}{l_2\times t_r}\right) \\ \frac{1}{6}\cdot\left(\frac{1}{l_1\times t_r}+\frac{1}{l_2\times t_r}\right) - \left|c_1(n_1,l_1,t_r) - c_2(n_2,l_2,t_{r2})\right| & , \quad 0 < \left|c_1(n_1,l_1,t_r) - c_2(n_2,l_2,t_{r2})\right| \le \frac{1}{6}\cdot\left(\frac{1}{l_1\times t_r}+\frac{1}{l_2\times t_r}\right) \\ \frac{1}{3}\cdot\min\left(\frac{1}{l_1\times t_r},\frac{1}{l_2\times t_r}\right) & , \quad \left|c_1(n_1,l_1,t_r) - c_2(n_2,l_2,t_{r2})\right| = 0 \end{cases} \tag{17}$$

Box I.

Where $c_1(n_1, l_1, t_r)$ is the central frequency of the n_1th noise-amplifying band of the first CCD pair, $c_2(n_2, l_2, t_r)$ is that of the n_2th noise-amplifying band of the second CCD pair, $w_{1,2}^{als}(n_1,n_2,l_1,l_2,t_r)$ denotes the aliasing bandwidth between $B_1(n_1, l_1, t_r)$ and $B_2(n_2, l_2, t_r)$, and the operator min(x, y) returns the smaller value of x and y. The maximal aliasing bandwidth equals to the width of the narrower noise-amplifying band.

4.2. Discussing the inevitable aliasing between two CCD pairs' noise-amplifying bands

Two CCD pairs generate two sets of noise-amplifying bands, for two noise-amplifying bands from different CCD pairs, they perhaps not alias with each other, while, for the entire two sets of noise-amplifying bands, aliasing may be inevitable. Here we put forward the following hypothesis: within jitter estimation bandwidth B_w, there is no aliasing between the entire two sets of noise-amplifying bands. If the hypothesis is not true, proving that the aliasing between the entire two sets is inevitable.

According to Eq. (6), Eqs. (13) and (17), the above hypothesis means that the inequality shown in Eq. (18) always holds.

$$\left|n_1\times F_1 - n_2\times F_2\right| > \frac{1}{6}(F_1+F_2), n_1 = 0,1,2,\ldots,\lfloor B_w/F_1\rfloor, \quad n_2 = 0,1,2,\ldots,\lfloor B_w/F_2\rfloor \tag{18}$$

Since F_1>0 and $F_2 = F_1/r$, Eq. (18) can be expressed as:

$$\left|n_1 - \frac{n_2}{r}\right| > \frac{1}{6}\left(1+\frac{1}{r}\right), n_1 = 0,1,2,\ldots,\lfloor B_w/F_1\rfloor, \quad n_2 = 0,1,2,\ldots,\lfloor B_w/F_2\rfloor \tag{19}$$

When $n_1 \le n_2/r$, since $r \ge 1$, Eq. (19) can be rewritten as

$$r < \frac{(n_2 - 1/6)}{(n_1 + 1/6)}, n_1 = 0, 1, 2, \ldots, \lfloor B_w/F_1 \rfloor, \quad n_2 = 0, 1, 2, \ldots, \lfloor B_w/F_2 \rfloor, n_1 \le \frac{n_2}{r} \tag{20}$$

Since the minimum of the expression on the right side of Eq. (20) is -1, if Eq. (18) holds for all n_1 and n_2, then r has to be less than -1, which is conflicts with the condition of $r \ge 1$, thus the above hypothesis does not always holds. Therefore, for two CCD pairs, it is inevitable for their entire two sets of noise-amplifying bands to alias with each other.

5. Extracting aliasing components from two CCD pairs' noise-amplifying bands

For two pairs of CCDs, their noise-amplifying frequencies can be divided into two categories: private noise-amplifying frequencies and aliasing noise-amplifying frequencies. Private noise-amplifying frequency refers to the noise-amplifying frequency only belonging to one CCD pair, while aliasing noise-amplifying frequency means the common noise-amplifying frequency of the two CCD pairs. Knowing the private frequencies of one pair allows us to remove the private frequencies' jitter results, and substitute them with the other pair's jitter results. Similarly, knowing the aliasing frequencies allows us to get rid of the corresponding jitter results of both the two pairs. So formulas are established to extract the aliasing and private components from two CCD pairs' noise-amplifying bands, as shown in Eq. (21)–(23).

$$B_{1,2}^{\text{als}}(n_1, n_2, l_1, l_2, t_r) = B_1(n_1, l_1, t_r) \cap B_2(n_2, l_2, t_r), \quad n_1 = 0, 1, 2, \ldots, \lfloor b_w \cdot l_1 \cdot t_r \rfloor, n_2 = 0, 1, 2, \ldots, \lfloor b_w \cdot l_2 \cdot t_r \rfloor \tag{21}$$

$$B_1^{\text{prv}}(n_1, n_2, l_1, l_2, t_r) = B_1(n_1, l_1, t_r) \cap \overline{B_1(n_1, l_1, t_r) \cap B_2(n_2, l_2, t_r)}, \quad n_1 = 0, 1, 2, \ldots, \lfloor b_w \cdot l_1 \cdot t \rfloor, n_2 = 0, 1, 2, \ldots, \lfloor b_w \cdot l_2 \cdot t_r \rfloor \tag{22}$$

$$B_2^{\text{prv}}(n_1, n_2, l_1, l_2, t_r) = B_2(n_2, l_2, t_r) \cap \overline{B_1(n_1, l_1, t_r) \cap B_2(n_2, l_2, t_r)}, \quad n_1 = 0, 1, 2, \ldots, \lfloor b_w \cdot l_1 \cdot t \rfloor, n_2 = 0, 1, 2, \ldots, \lfloor b_w \cdot l_2 \cdot t_r \rfloor \tag{23}$$

Where $B_1(n_1, l_1, t_r)$ is the n_1th noise-amplifying band of the first CCD pair, and $B_2(n_2, l_2, t_r)$ is the n_2th noise-amplifying band of the second CCD pair, B als 1,2 $(n_1, n_2, l_1, l_2, t_r)$ denotes the aliasing noise-amplifying band between $B_1(n_1, l_1, t_r)$ and $B_2(n_2, l_2, t_r)$, Bprv 1 $(n_1, n_2, l_1, l_2, t_r)$ represents the private components of the first CCD pair in $B_1(n_1, l_1, t_r)$, and Bprv 2$(n_1, n_2, l_1, l_2, t_r)$ is the private components of the second CCD pair in $B_2(n_2, l_2, t_r)$.

According to Section 4.1, for two noise-amplifying bands from different CCD pairs, aliasing will occur if the two bands' center interval is less than half of their total bandwidth, and two closer noise-amplifying bands make a wider aliasing band. As a result, the aliasing bandwidth reaches its maximum where its two original noise-amplifying bands share the same center, and gradually decreases as the two original bands move away from each other, until to zero (not aliased), and such repeats. The periodicity of aliasing bandwidth will be demonstrated in the following experiments section. Here we explore how to determine the period of aliasing bandwidth.

Since the center of a noise-amplifying band is located at an integral multiple of its CCD pair's fundamental frequency, two bands' shared center appears at those common multiples of the two CCD pairs' fundamental frequencies. At the same time, the widest aliasing bandwidth occurs at the shared center. Therefore, the widest aliasing bandwidth occurs at those common multiples of its two original CCD pairs' fundamental frequencies, namely $n_1 \times F_1 = n_2 \times F_2$, where n_1 and n_2 are non-negative integers, F_1 and F_2 are the two CCD pairs' fundamental frequencies. According to Eq. (17), the widest aliasing bandwidth can be written as Eq. (24)

$$\max\left[w_{1,2}^{\text{als}}(n_1, n_2, l_1, l_2, t_r)\right] = \frac{1}{3} \cdot \min\left(\frac{1}{l_1 \times t_r}, \frac{1}{l_2 \times t_r}\right) = \frac{1}{3} \cdot \min\left(F_1, F_2\right), \quad when\, n_1 \times F_1 = n_2 \times F_2 \tag{24}$$

The period length of aliasing bandwidth equals to the least common multiple of the two CCD pairs' fundamental frequencies, as shown in Eq. (25).

$$p_{1,2}^{\text{als}}(l_1, l_2, t_r) = \text{lcm}\left(\frac{1}{l_1 \times t_r}, \frac{1}{l_2 \times t_r}\right) = \text{lcm}\left(F_1, F_2\right) = \frac{1}{l_1 \cdot t_r} \times \text{lcm}_r(r) = F_1 \times \text{lcm}_r(r), \quad r = \frac{l_2}{l_1} \tag{25}$$

Where $p_{1,2}^{als}(l_1, l_2, t_r)$ denotes the period length of aliasing bandwidth, l_1 denotes the distance between the first lines of the first CCD pair, l_2 denotes that of the second CCD pair, and t_r means the image line time of two CCD pairs, F_1 and F_2 denote the two CCD pairs' fundamental frequencies, the operator lcm(F_1, F_2) finds two coprime positive integers n_1 and n_2 that satisfy $n_1 \times F_1 = n_2 \times F_2$, and returns the value of $n_1 \times F_1$, the operator lcm$_r(r)$ finds two coprime positive integers whose ratio is r, and returns the smaller one.

It is worth noting that, in mathematics, the least common multiple is specific to positive integers. However, in this study, fundamental frequencies are probably not integers, but they must be rational numbers, so we expand the concept of least common multiple to rational numbers. Just like the noise-amplifying bands of two adjacent CCDs, the aliasing bands of three adjacent CCDs are also determined by the three CCDs' layout parameter values and their image line time.

6. Experiments and results discussion

This section is divided into two parts. Firstly, for one CCD pair, numerical simulations and experiments on Chinese xx-1 satellite are performed to test the established formulas for determining ETC and noise-amplifying bands in jitter detection. Secondly, for two pairs of CCDs formed by three adjacent CCDs, numerical simulations are conducted to examine the periodicity of aliasing bandwidth between the two CCD pairs' noise-amplifying bands.

6.1. Results of noise-amplifying bands for one CCD pair

Due to lack of on-orbit satellite jitter's true values, it is difficult to evaluate the jitter error and the transfer coefficients between jitter error and offset noise. Nevertheless, experiments performed on an on-orbit satellite jitter still allow to confirm the existence of noise-amplifying bands in jitter estimation and their periodicity. By contrast, numerical simulations prove an access to accurate jitter error, which enables us to calculate the error transfer coefficients, and eventually test the constructed theories determining noise-amplifying bands in jitter estimation.

6.1.1. Numerical simulations

The established formulas are functions of CCD parameters of l and t_r, l denotes the distance between two adjacent CCDs' first lines, and t_r represents the two CCDs' image line time. The parameter l and t_r are both set within reasonable value ranges and sampled at small steps to go through all possible cases. The distance between two adjacent CCDs' first lines depends on CCDs' house size, which is typically thousands of pixels size, for example, two adjacent CCDs in Chinese xx-1 satellite is 3480 lines apart from each other. So the CCD layout parameter l is set within 1000~20000 lines with a step of 100 lines. CCD's image line time relies on its pixels size and satellite's orbital altitude, for example, HiRISE satellite's image line time is typically 100 μs, and the most representative image line time on Chinese xx-1 satellite is 65 μs. So CCD's image line time t_r is set to be 50~300 μs with a step of 10 μs. White noise was used to simulate the true jitter, offset data were then mixed with white noise σ_{offset}, and the corresponding jitter was finally estimated by using the method in [26]. Following this,

discrete Fourier transform was performed on offset data noise and the deviations between the jitter results and its true values, and the ratio of the amplitudes between offset data noise and jitter deviations are used to calculate ETC. For each set of l and t_r values, 50 times are repeated to obtain 50 ETC results. The maximal and minimal ETC values are removed and the rest is used to calculate an average value. As a result, nearly 5,000 ETC values are obtained.

Before showing all the ETC results, three of them are selected to demonstrate how ETC periodically varies with frequencies. Parameters are as follows: example1: l = 2400 lines, t_r = 140 μs; example2: l = 5300 lines, t_r = 100 μs; example3: l = 8800 lines, t_r = 90 μs. Theoretically, ETC is a periodic function of frequency, and its period length equals to the fundamental frequency of its CCD pair, which are 2.9762 Hz, 1.8868 Hz and 1.2626 Hz in the three examples. ETC results in the three examples are shown in Fig. 8(a)–(c). The green dots and blue curves represent the ETC results from simulations and its values calculated by the established formula (only curves within 20 Hz are displayed for easy observation). The ETC results from simulations are basically consistent with its values from ETC formula, and show an obvious periodical pattern. In each period, the ETC results are axisymmetric around its central frequency (marked by red triangles), where reach infinity and gradually decrease as frequencies move away from the center, which agrees with the theoretical analysis in Section 3.1. In addition, central frequencies increases linearly, as shown in Fig. 8(d)–(f). The slope of the central frequency line is adopted to compute the ETC's period, which are 2.9762 Hz, 1.8868 Hz and 1.2626 Hz, equivalent to the above three fundamental frequencies. Theoretically, the ETC within a cycle intersects with the line ETC = 1 at two points, but in reality, the ETC turned out to be large numbers of discrete points distributed near their theoretical values, as shown in Fig. 8(a), among which bad points were first removed and the rest points were then smoothed to obtain a smoother curve of the ETC results. Following this, the two points where the ETC curve within a cycle intersected with the line ETC =1 were determined and the difference between them was regarded as the bandwidth a noise-amplifying band spans. For each value set of l and t_r, the bandwidths of all noise-amplifying bands are theoretically equal, while the actual noise-amplifying bands have different bandwidths, as shown in Fig. 8(g)–(i), the red diamonds and blue stars represent the bandwidth values from the established formula and its actual results from simulations, respectively. The average of all the actual bandwidth values is used to be the final bandwidth value. Unlike the central frequencies of noise-amplifying bands, their bandwidth results deviate from their theoretical values (discussions are given in Section 7). Firstly, for each set of l and t_r values, the ETC peak frequency in a noise-amplifying band is regarded as its center, just like the red triangle in Fig. 8(a). All the center values from simulations and that from the built formula are used to calculate their deviations, which are then adopted to compute a RMSE. Large numbers of simulations were conducted to obtain nearly 5,000 RMSE data, as shown in Fig. 9(a). All the RMSE data is used to compute a room mean square, and it is regarded as the final RMSE to evaluate the performance of built formula. As a result, the final RMSE is as low as 7.127×10^{-5} Hz, as show in Table 2. It can be seen that the established equations could provide a reliable results for central frequencies of a noise-amplifying band.

Secondly, two adjacent central frequencies are used to calculate their difference, and the average difference is taken as the period length of a noise-amplifying band. Results are shown by the red dots in Fig. 9(b), and their fitted surface can be expressed as Eq. (26) ($R^2 = 1$), which is exactly the same as the established Eq. (12). The relative deviations between the period values from simulations and their values from the built formula are employed to calculate relative root mean square error (RRMSE), as shown in Fig. 9(c). RRMSE is as low as 0.0051%, as show in Table 2. Therefore, it is proved that the established formula could generate an accurate ETC period result.

$$p_n(l,t_r)_{fit} = \frac{1}{l\times t_r} \tag{26}$$

Finally, bandwidth results are shown in Fig. 9(d), and their fitted surface can be written as Eq. (27) ($R^2 = 0.9998$). There is some difference between the fitted equation and its theoretical formula Eq. (14) (Since the 0th period length in simulations was removed, so the fitted equation only shows the period length with n>0). Fig. 9(e) shows the relative deviations of bandwidths between their values from simulations and their values from the built formula, and RRMSE is 1.2610%, as show in Table 2. Compared with the central frequencies of noise-amplifying bands, their bandwidths deviate from its theoretical value more severely, and more details are discussed in Section 7.

$$w\left(n,l,t_r\right)_{fit} = \frac{0.3304}{l\times t_r}, \quad n = 1,2,3,\ldots \tag{27}$$

6.1.2. Experiments on satellite jitter estimation

In Section 2, experiments on Chinese xx-1 satellite jitter estimation are performed to provide an evidence for noise-amplifying problems in jitter detection, and two questions are raised. Here we employ the constructed theories to analyze the questions in Section 2.

For Chinese xx-1 satellite with image line time t_r of 65 μs and two adjacent CCDs' first lines distance l of 3480 lines, their ETC and blind frequencies are calculated by using Eqs. (7) and (8). Fig. 10 compares the satellite jitter values from experiments (red curves) and its ETC values from the built formulas (blue curves), and their peaks are marked by red and blue triangles. Since most of the satellite jitter energy is concentrated in the lower frequencies, the amplitudes at lower frequencies are larger than that at higher ones. Theoretically, with the satellite image line time t_r of 65 microseconds and interval l of 3480 lines, its fundamental frequency is 4.42 Hz, and the satellite's noise-amplifying bands are expected to be located around the central frequencies of integer multiples of 4.42 Hz, meaning 0 Hz, 4.42 Hz, 8.84 Hz, 13.26 Hz, 17.68 Hz, *etc*., while they turn out to be at 0.05 Hz, 4.38 Hz, 8.81 Hz, 13.27 Hz, 17.64 Hz in cross-track direction, *etc*., as shown in Fig. 10(a) and Fig. 10(c), and the RRMSE between the central frequencies results and their theoretical values is 0.1672% in cross-track direction. Similarly, the satellite jitter in down-track direction is shown in Fig. 10(d)–Fig. 10(f), and the RRMSE of central frequencies is 0.1310%. It can be seen that blind frequencies and noise-amplifying bands do exist in satellite jitter estimation and they reappear periodically, which is consistent with the above theoretical analysis.

6.2. Results of aliasing between two CCD pairs' noise-amplifying bands

Numerical simulations were conducted to test the periodicity of aliasing between two CCD pairs' noise-amplifying bands, and prove the correctness of the established formula for computing aliasing period. For two pairs of CCDs with their specific fundamental frequencies of F_1 and F_2(let $F_1 \geq F_2$ and $r = F_1/F_2$), their aliasing period relays on the fundamental frequency F_1 and the ratio r according to Eq. (25). Just like the simulations in Section 6.1, let the distance l_1 in the range of 1000–20000 lines with a step of 100 lines, and the image line time t_r in the range of 50~300 μs with a step of 10 μs. So the fundamental frequency F_1 is set in the value range of 0.16~20 Hz with a step of 0.2 Hz ($F_{1u}=1/(l_1\times t_r)=1/(1000\times50\times10^{-6})=20$ Hz, and $F_{1u}=1/(l_1\times t_r)=1/(20000\times300\times10^{-6}) \approx 0.16$ Hz). It was noticed in our previous work that the number of aliasing noise-amplifying bands would rise rapidly if r exceeded 2, causing difficulties in subsequent aliasing bandwidth minimization, so we set the ratio r in a reasonable range of 1–2 with a step of 0.01. For each set of values of F_1 and r, the aliasing noise-amplifying bands were calculated by using Eq. (21), its period is estimated by observing the envelope of aliasing bandwidth curves.

Fig. 11 compares the aliasing period values from simulation results (the red dots in Fig. 11(a) and Fig. 11(b)) with its values calculated by the established formula (the surface in Fig. 11(a) and Fig. 11(b)). The deviation between them is employed to calculate RMSE and RRMSE, as shown in Fig. 11(c). RMSE and RRMSE are 0.0030 Hz and 0.0033%,

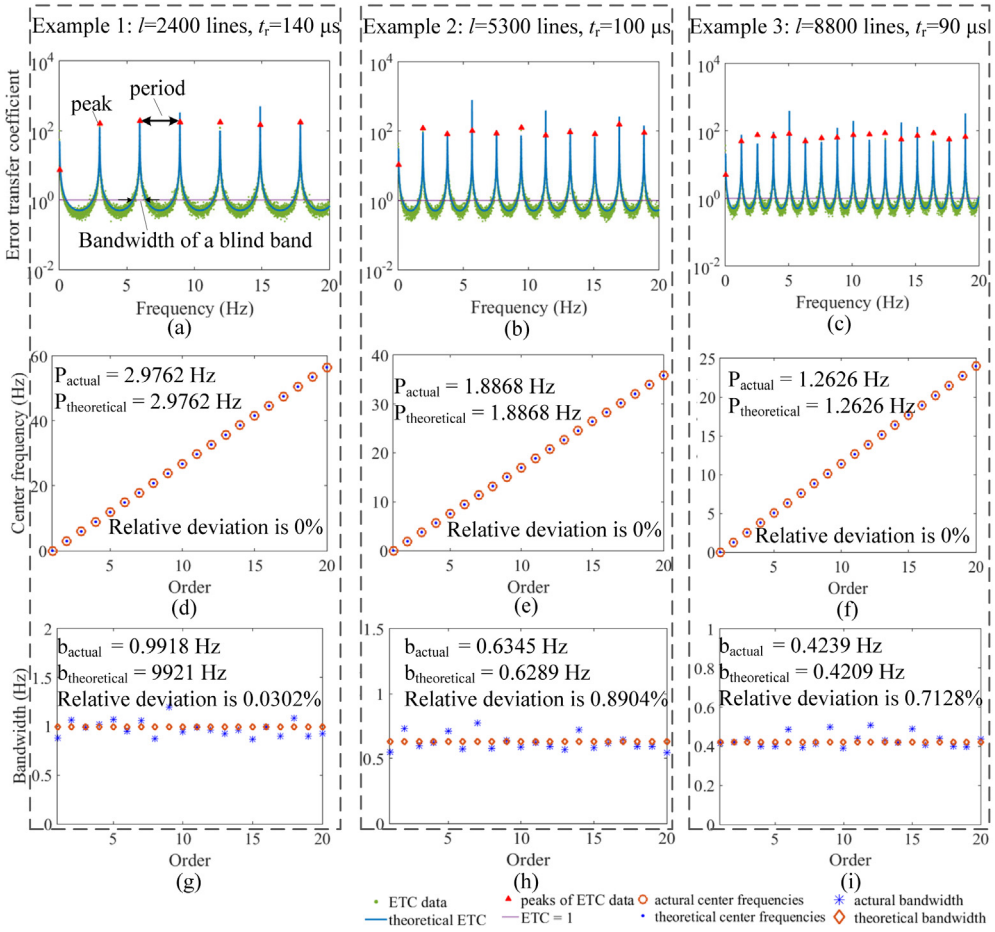

Fig. 8. Three examples to demonstrate the periodicity of error transfer coefficient. Error transfer coefficients of (a) Example 1, (b) Example 2 and (c) Example 3. Center frequencies of (d) Example 1, (e) Example 2 and (f) Example 3. Bandwidth of each noise-amplifying band of (g) Example 1, (h) Example 2 and (i) Example 3.

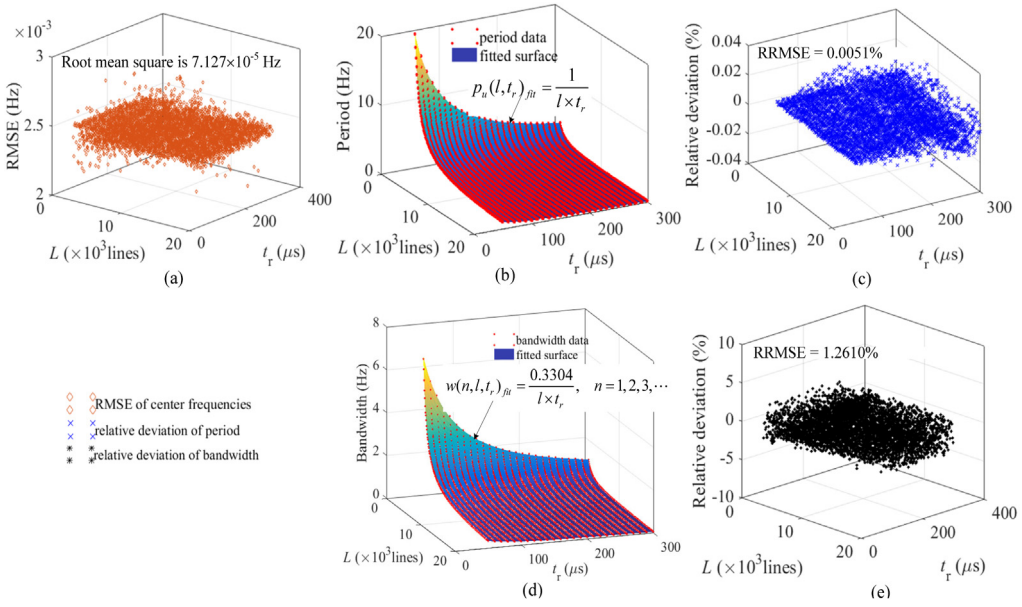

Fig. 9. Comparison between results from simulations and those values from the built formulas. (a) Central frequencies' RMSE. (b) Noise-amplifying band's period results from simulations and their fitted surface. (c) Relative deviations of noise-amplifying bands' periods. (d) Noise-amplifying bands bandwidth results from simulations and their fitted surface. (e) Relative deviations of noise-amplifying bands bandwidth.

Table 2
Simulations results of two adjacent CCDs' noise-amplifying bands.

	Established formula	Fitted formula	RMSE/RRMSE
Central frequency	$c\left(n,l,t_r\right)=\frac{n}{l\times t_r}, n=1,2,3,\ldots$	–	7.127×10^{-5} Hz
Period	$p_n(l,t_r)=\frac{1}{l\times t_r}$	$p_n(l,t_r)_{fit}=\frac{1}{l\times t_r}$	0.0051%
Bandwidth	$w(n,l,t_r)=\frac{1}{3\times l\times t_r}, n=1,2,3,\ldots$	$w(n,l,t_r)_{fit}=\frac{0.3304}{l\times t_r}, n=1,2,3,\ldots$	1.2610%

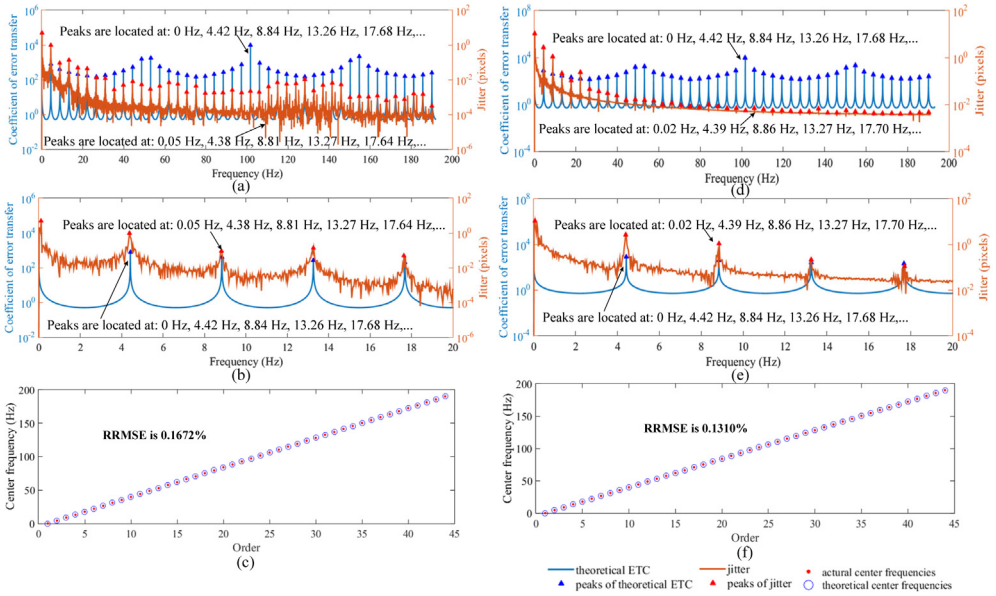

Fig. 10. Comparison between satellite jitter results and theoretical ETC. (a) Frequency-domain comparison in 0–192 Hz in cross-track direction. (b) 0–20 Hz part of Fig. 10(a). (c) Central frequencies of noise-amplifying bands in cross-track direction. (d) Frequency-domain comparison in 0–192 Hz in down-track direction. (e) 0–20 Hz part of Fig. 10(d). (f) Central frequencies of noise-amplifying bands in down-track direction.

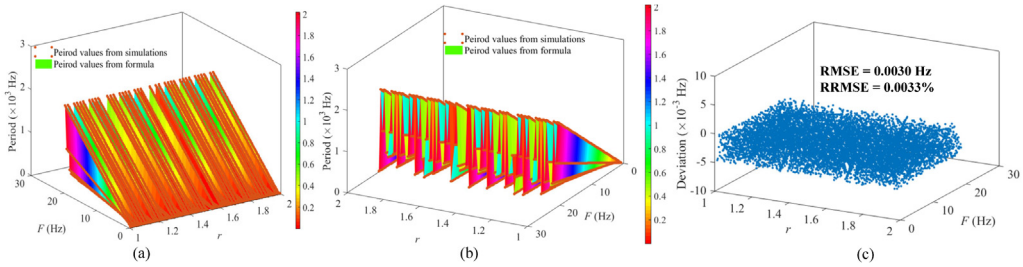

Fig. 11. Comparisons of aliasing period between simulation results and theoretical values. (a) Front view. (b) Rear view. (c) Deviation between simulations results and theoretical values.

respectively. It can be seen that the established formula can provide an effective results for aliasing period between two CCD pairs' noise-amplifying bands. In addition, larger F_1 produces a larger period, as shown in the front view Fig. 11(a), while the period does not show any obvious pattern as r varies, as shown in the rear view Fig. 11(b), which is consistent with the established formula Eq. (25).

In order to visually demonstrate the periodicity of aliasing bandwidth, we select four groups of results (Fig. 12(a)–(d)), where F_1 and r are respectively set with a larger value and a smaller value in their specific ranges. Fig. 12(e)–(h) are the details of Fig. 12(a)–(d). It can be seen that aliasing bandwidth shows obvious periodicity. However, it should be noticed that, in some cases, there is a clear boundary between two aliasing periods, as shown in Fig. 12(a) and its details Fig. 12(e), Fig. 12(b) and its details Fig. 12(f), while more often than that, two cycles intersect with each other on their borders, as shown in Fig. 12(c) and its details Fig. 12(g), Fig. 12(d) and its details Fig. 12(h), which bring challenges to minimize aliasing bandwidth between two CCD pairs' noise-amplifying bands and will be the focus of our follow-up research.

7. Discussions

The simulation results in Section 6.1 show that the RRMSE is 1.2610% for bandwidth formula, while 0.0051% for central frequency formula. Here we discuss why the simulation result of bandwidth deviates from its theoretical values more seriously than that of central frequency does.

According to Eq. (7), ETC $\kappa(F,f)$ varies with frequencies, and it can be expressed in two cases, as shown in Eq. (28).

$$\kappa\left(F,f\right)=\left|\frac{1}{2\sin\left(\frac{\pi\cdot f}{F}\right)}\right|$$

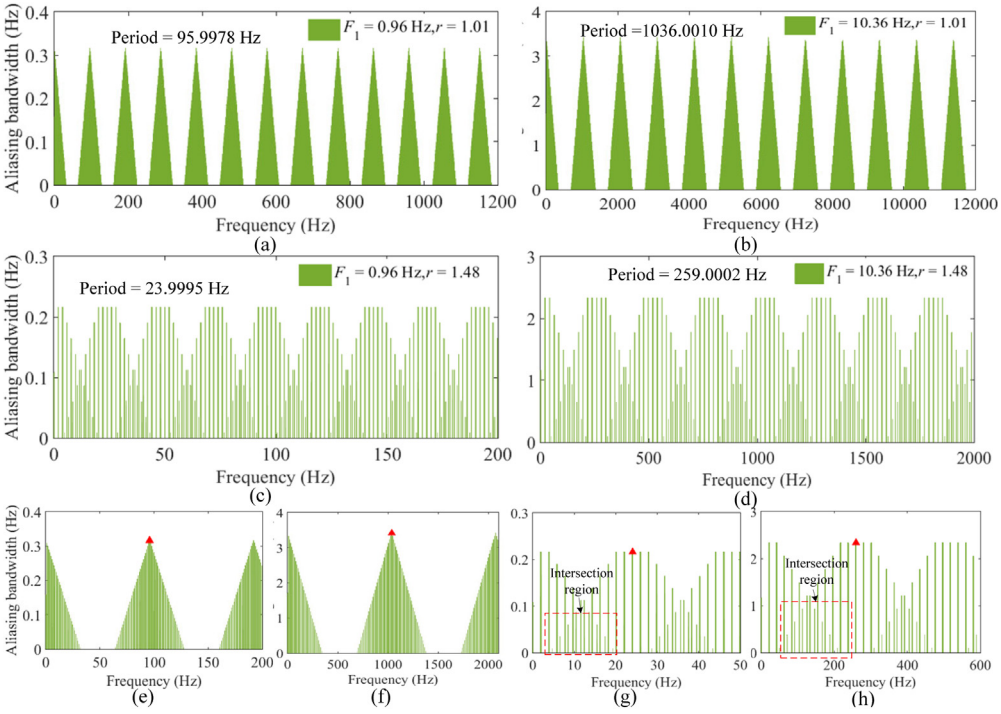

Fig. 12. Results of aliasing bandwidth between two CCD pairs' noise-amplifying bands under some specific values of F_1 and r (F_1=1/l_1/t_t, $r = l_2/l_1 = F_1/F_2$). Aliasing bandwidth in the cases of (a) F_1 = 0.96 Hz and r = 1.01 (F_2 = 0.9696 Hz). (b) F_1 = 10.36 Hz and r = 1.01 (F_2 = 10.4636 Hz). (c) F_1 = 0.96 Hz and r = 1.48 (F_2 = 1.4208 Hz). (d)F_1 = 10.36 Hz and r = 1.48 (F_2 = 15.3328 Hz). (e) Details of Fig. 12(a). (f) Details of Fig. 12(b). (g) Details of Fig. 12(c). (h) Details of Fig. 12(d).

$$= \begin{cases} \dfrac{1}{2\sin\left(\frac{\pi\cdot f}{F}\right)}, & 2(n-1)F < f < 2nF - F,\ n = 1,2,3,\ldots \\ \dfrac{-1}{2\sin\left(\frac{\pi\cdot f}{F}\right)}, & 2nF - F < f < 2nF,\ n = 1,2,3,\ldots \end{cases} \tag{28}$$

Where F denotes the CCD pair's fundamental frequency. Then the derivative of $\kappa(F, f)$ with respect to f can be written as:

$$\kappa'(F,f) = \frac{\partial \kappa(F,f)}{\partial f} = \begin{cases} -\dfrac{\pi}{2F} \times \dfrac{\cos\left(\frac{\pi\cdot f}{F}\right)}{\sin\left(\frac{\pi\cdot f}{F}\right)^2}, & 2(n-1)F < f < 2nF - F,\ n = 1,2,3,\ldots \\ \dfrac{\pi}{2F} \times \dfrac{\cos\left(\frac{\pi\cdot f}{F}\right)}{\sin\left(\frac{\pi\cdot f}{F}\right)^2}, & 2nF - F < f < 2nF,\ n = 1,2,3,\ldots \end{cases} \tag{29}$$

In the cases where f approaches an integer multiple of F, namely $f \to n\times F$, n = 0, 1, 2, …, the derivative of ETC reaches infinity, as shown in Eq. (30).

$$\lim_{f\to nF} \kappa'(F,f) = \pm\infty \tag{30}$$

When ETC=1, the frequency f can be expressed as:

$$f = \begin{cases} 1/6 \times F, & n = 0 \\ (n \pm 1/6) \times F, & n = 1,2,3,\ldots \end{cases} \tag{31}$$

The corresponding derivative of ETC equals to:

$$\lim_{ETC=1} \kappa'(F,f) = \pm\sqrt{3}\frac{\pi}{F} \tag{32}$$

It can be seen that the absolute value of the derivative at ETC=1 is much less than that at the frequency approaching an integer multiple of F, namely $f \to n\times F$, n = 0, 1, 2, …, and the corresponding ETC→∞, as shown in Eq. (33).

$$\left|\lim_{ETC=1} \kappa'(F,f)\right| \ll \left|\lim_{f\to nF} \kappa'(F,f)\right| = \left|\lim_{ETC\to\infty} \kappa'(F,f)\right|, \quad n = 0,1,2,\ldots \tag{33}$$

The ETC data from simulations contains large numbers of discrete points which are located near their theoretical values, as shown in Fig. 13(a). Bad points are first removed and smoothing is then used to obtain a smoother ETC curve. In a noise-amplifying band, the smoothed ETC curve intersects with the line ETC =1 at two points, and the difference between the two points' frequencies is regarded as the bandwidth estimated value, as shown by the blue double arrows in Fig. 13(b). The peak of the ETC discrete points in a noise-amplifying band is used as its center frequency, as shown by the red triangles in Fig. 13(b).

Since the absolute value of the derivative at ETC=1 is much less than that around ETC→∞, more discrete points gather around ETC=1, while very few points appear around ETC→∞, as shown in Fig. 13(a). Even after smoothing the ETC data, the standard deviation around ETC=1 is still much larger than that around ETC→∞, namely $\sigma_{ETC=1} > \sigma_{ETC\to\infty}$, as shown in Fig. 13(b). As a result, the RRMSE for the bandwidth estimated values is much larger than that for the central frequency estimated values.

8. Conclusion

This research discoveries the noise-amplifying issues in satellite jitter detection, and constructs theories to determine the noise-amplifying frequencies, find out what patterns they follow, and investigate what CCD parameters determine them. Numerical simulations and experiments on a Chinese satellite were conducted to test the performance of the constructed theories. Conclusions can be made as follow.

(1) A formula is established to compute the transfer coefficient between jitter error and offset data noise. Simulation results are basically consistent with the theoretical ETC values, proving the

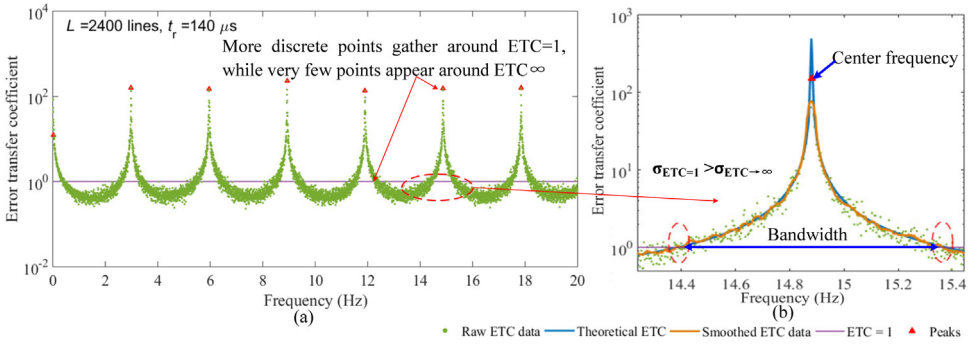

Fig. 13. Comparisons between ETC=1 and ETC→∞. (a) The number of ETC data points comparisons between ETC=1 and ETC→∞. (b) Standard deviation of the smoothed ETC curve comparisons between ETC=1 and ETC→∞.

correctness of the established ETC formula. Besides, both the established formula and simulation results indicate that the ETC is a periodic function of frequency, and in each cycle, the ETC is axisymmetric around its central frequency, reaches infinity at its center and gradually decreases as the frequencies move away from its center.

(2) For two adjacent CCDs, formulas are established to determine the blind frequencies and noise-amplifying bands, calculate their period length, and locate the center frequency and bandwidth of a noise-amplifying band. Simulation results show that RMSE is as low as 7.127×10^{-5} Hz for the central frequencies formula, RRMSE is 0.0051% for the period formula. By contrast, RRMSE is 1.2610% for the bandwidth formula, which is larger than that of central frequencies. But fortunately, the RRMSE of ~1% has little effect on the subsequent noise-amplifying frequencies elimination based on filter design. In addition, experimental results performed on Chinese xx-1 satellite jitter estimation confirm the existence of noise-amplifying bands and their periodic pattern. So it is proved that the established formulas could provide reliable results for blind frequencies and noise-amplifying bands.

(3) It is the two CCDs' image line time t_r and the distance l between the two CCDs' first lines that determine the blind frequencies and noise-amplifying bands in detected jitter results. The reciprocal of the product of t_r and l is defined as the fundamental frequency F of the CCD pair. As a results, the blind frequencies and noise-amplifying bands both reoccur with a period of fundamental frequency F, but unlike the isolated blind frequencies, the noise-amplifying band spans much wider band up to 1/3 F, thereby all the noise-amplifying bands total up to nearly 1/3 jitter bandwidth.

(4) Three adjacent CCDs form two CCD pairs and generate two sets of noise-amplifying bands. Aliasing between the two sets of noise-amplifying bands is first proven to be inevitable. Formulas are then established to extract the aliasing components from two CCD pairs' noise-amplifying bands, which indicates that the aliasing reoccur periodically and its period length is determined by the two CCD pairs' fundamental frequencies. Simulation results show that the aliasing period length's RMSE and RRMSE are 0.0030 Hz and 0.0033%, respectively, proving that the established equation could provide an effective results for aliasing period.

In conclusion, for three adjacent CCDs whose parallax observation images are used to detect satellite jitter, it is the distances between the CCDs' first lines and their image line time that determine the blind frequencies, noise-amplifying bands and their aliasing components in jitter detection. The constructed theories are expected to help analyze more CCD pairs' noise-amplifying issues and provide a prospect to reduce their impact on jitter detection by optimizing CCD parameter values.

Funding

National Natural Science Foundation of China (NSFC) (Grant No. 61805001, 61905002); Natural Science Foundation of Anhui Province, China (Grant No. 1808085QF218); Open Research Fund of Anhui Provincial Key Laboratory of Smart Agricultural Technology and Equipment, China (Grant No. APKLSATE2019X007); Natural Science Research Projects in Anhui Universities, China (Grant No. KJ2019A0210); Open Research Fund of National Engineering Research Center for Agro-Ecological Big Data Analysis & Application, Anhui University, China (No. AE201905).

Declaration of competing interest

The authors declare that they have no known competing financial interests or personal relationships that could have appeared to influence the work reported in this paper.

Acknowledgments

The authors thank the editors and the reviewers for their constructive and helpful comments, and also thank the Changchun Institute of Optics, Fine Mechanics and Physics for the efforts in experiments.

References

[1] S. Roques, L. Jahan, B. Rougé, C. Thiebaut, Satellite attitude instability effects on stereo images, in: Proceedings of IEEE Conference on Acoustics, Speech and Signal Processing, IEEE, 2004, pp. 477–480.
[2] Y. Li, X. Wang, Z. Wang, D. Liu, Y. Ding, Modeling and image motion analysis of parallel complementary compressive sensing imaging system, Opt. Commun. 243 (2018) 100–110.
[3] M. Wang, C. Fan, J. Pan, S. Jin, X. Chang, Image jitter detection and compensation using a high-frequency angular displacement method for Yaogan-26 remote sensing satellite, ISPRS J. Photogramm. Rem. Sens. 130 (2017) 32–43.
[4] H. Liu, H. Ma, Z. Jiang, Algorithm of satellite platform jitter estimation for the period of non-overlapping images, Acta Opt. Sin. 39 (5) (2019) 0512002.
[5] T. Sun, H. Long, B.C. Liu, Application of attitude jitter detection based on short-time asynchronous images and compensation methods for Chinese mapping satellite-1, Opt. Express 23 (2) (2015) 1395.
[6] H. Liu, S. Xu, D. Wang, Space camera image motion measurement based on images from time delayed integration sensors overlapped area, Acta Opt. Sin. 34 (2) (2014) 0212001-1-0212001-7.
[7] F. Ayoub, S. Leprince, R. Binety, K.W. Lewis, O. Aharonson, J.P. Avouac, Influence of Camera Distortions on Satellite Image Registration and Change Detection Applications, IGARSS, 2008, II-1072–II-1075.
[8] H. Liu, D. Wang, D. Yan, S. Xu, Study on blind band elimination in jitter estimation, Chin. Opt. Lett. 12 (10) (2014) 101203-101207.
[9] A. Mcewen, M. Banks, N. Baugh, K. Becker, A. Boyd, J.W. Bergstrom, The high resolution imaging science experiment (HiRISE) during MRO's primary science phase (PSP), Icarus 205 (1) (2010) 2–37.
[10] P. Sabelhaus, J. Bolek, S. Scott, E. Holmes, R. James, On-orbit ACDS performance of the Landsat 7 spacecraft, in: Proceedings of AAS Guidance and Control, 2001.
[11] J. Lu, M. Hu, Y. Yang, et al., On-Orbit calibration method for redundant IMU based on satellite navigation & star sensor information fusion, IEEE. Sens. J. (99) (2020) 1.

[12] K. Janschek, V. Tchernykh, S. Dyblenko, Integrated camera motion compensation by real-time image motion tracking and image deconvolution, in: International Conference on Advanced Intelligent Mechatronics, 2005, pp. 1437–1444.
[13] V. Tchernykh, M. Beck, K. Janschek, Optical Correlator Based Optical Flow Processor for Real Time Visual Navigation, InTech Open Access Publisher, 2007, pp. 223–236.
[14] K. Janschek, V. Tchernykh, S. Dyblenko, Performance analysis of opto-mechatronic image stabilization for a compact space camera, Control Eng. Pract. 15 (3) (2007) 333–347.
[15] S. Mattson, A. Boyd, R.L. Kirk, HiJACK: Correcting spacecraft jitter in HiRISE images of Mars, Health Manage. Technol. 33 (5) (2009) A162.
[16] S. Mattson, A. Bartels, A. Boyd, Continuing analysis of spacecraft jitter in LROC-NAC, Am. Nat. 152 (3) (2011) 321–337.
[17] X. Tong, Y. Xu, Z. Ye, S. Liu, X. Tang, L. Li, H. Xie, J. Xie, Attitude oscillation detection of the ZY-3 satellite by using multispectral parallax images, IEEE Trans. Geosci. Rem. Sens. 53 (6) (2015) 3522–3534.
[18] X. Tong, L. Li, S. Liu, Y. Xu, Z. Ye, Y. Jin, F. Wang, H. Xie, Detection and estimation of ZY-3 three-line array image distortions caused by attitude oscillation, ISPRS J. Photogramm. Rem. Sens. 101 (10) (2015) 291–309.
[19] Z. Ye, Y. Xu, X. Tong, S. Zheng, H. Zhang, H. Xie, U. Stillaand, Estimation and analysis of along-track attitude jitter of ZiYuan-3 satellite based on relative residuals of tri-band multispectral imagery, ISPRS J. Photogramm. 158 (2019) 188–200.
[20] Y. Teshima, A. Iwasaki, Correction of attitude fluctuation of terra spacecraft using ASTER/SWIR imagery with parallax observation, IEEE Trans. Geosci. Rem. Sens. 46 (1) (2008) 222–227.
[21] A. Iwasaki, Detection and estimation satellite attitude jitter using remote sensing imagery, in: J. Hall (Ed.), Advances in Spacecraft Technologies, Vol. 13, InTech, Rijeka, Croatia, 2011, pp. 257–272.
[22] T. Sun, H. Long, B.C. Liu, Y. Li, Application of attitude jitter detection based on short-time asynchronous images and compensation methods for Chinese mapping satellite-1, Opt. Express 23 (2) (2015) 1395.
[23] R. Mumtaz, P. Palmer, Attitude determination by exploiting geometric distortions in stereo images of DMC camera, IEEE Trans. Aerosp. Electron. Syst. 49 (3) (2013) 1601–1625.
[24] S. Liu, X. Tong, F. Wang, W. Sun, C. Guo, Z. Ye, Y. Jin, H. Xie, P. Chen, Attitude jitter detection based on remotely sensed images and dense ground controls: a case study for Chinese ZY-3 satellite, IEEE J. Sel. Top. Appl. Earth Observ. 9 (12) (2016) 5760–5766.
[25] Y. Zhu, M. Wang, Y. Cheng, L. He, L. Xue, An improved jitter detection method based on parallax observation of multispectral sensors for gaofen-1 02/03/04 satellites, Remot. Sens. 11 (1) (2019) 16.
[26] H. Liu, H. Ma, Z. Jiang, D. Yan, Jitter detection based on parallax observations and attitude data for Chinese Heavenly Palace-1 satellite, Opt. Express 27 (2) (2019) 1099–1123.
[27] A.S. Mcewen, E.M. Eliason, J.W. Rgstrom, Mars reconnaissance orbiter's high resolution imaging science experiment (HiRISE), J. Geophys. Res.-Atmos. 112 (E5) (2007) 5.
[28] S. Velichko, V. Korokhin, Y. Velikodsky, Removal of topographic effects from LROC NAC images as applied to the inner flank of the crater Hertzsprung S, Planet Space Sci. 193 (1) (2020) 105090.
[29] Y. Chen, X. Zhong, Z. Qiu, Calibration and validation of ZY-3 optical sensors, IEEE Trans. Geosci. Remote Sens. 53 (8) (2015) 4616–4626.
[30] H. Fujisada, Design and performance of ASTER instrument, Proc. SPIE Int. Soc. Opt. Eng. (1995) 2583.
[31] H. Liu, High Resolution Space Camera Image Motion Measurement Based on Images from TDICCD Overlapping Area, Chinese Academy of Sciences University, 2015.